Biomedical Physics &
Engineering Express

Endorsed by IPEM Institute of Physics and Engineering in Medicine
PURPOSE-LED PUBLISHING™

PAPER • **OPEN ACCESS**

Simulations of a new PET scanner for 3D proton therapy quality assurance

To cite this article: A C M Magalhães *et al* 2025 *Biomed. Phys. Eng. Express* **11** 065037

View the article online for updates and enhancements.

You may also like

- Mathematical modelling of magnetic field and nanoparticle effects on calcium signalling in malignant esophageal cells
Yevhen Salatskyi, Svitlana Gorobets and Oksana Gorobets
- Torso synthetic CT generation by integrating deep learning and segmentation for FDG-PET/MR attenuation correction
Jin Uk Heo, Shujin Sun, Robert S Jones et al.
- CSCST-Net: a fully sparse-regularized convolutional sparse coding network for low-dose CT denoising
Jinxin Luo, Yi Liu, Tao Wang et al.





GAS

BreathSpec®

The combination of GC and IMS enables a physical separation to detect volatiles without pre-concentration directly sampled from human breath.

Our GC-IMS based analyzer allows instant breath sampling and analysis of volatiles in minutes.

The transportable GC-IMS facilitates versatile sampling incl. direct exhalation, syringe based and also gas bags for sampling of breath and static body headspace (oral/nasal/skin).

▶▶▶ click for more details

This content was downloaded from IP address 15.204.172.50 on 06/11/2026 at 10:31

Biomedical Physics & Engineering Express

Check for updates

PAPER

OPEN ACCESS

RECEIVED
31 July 2025

REVISED
8 October 2025

ACCEPTED FOR PUBLICATION
24 October 2025

PUBLISHED
6 November 2025

Original content from this work may be used under the terms of the Creative Commons Attribution 4.0 licence.

Any further distribution of this work must maintain attribution to the author(s) and the title of the work, journal citation and DOI.

Simulations of a new PET scanner for 3D proton therapy quality assurance

A C M Magalhães* , P M M Correia , P M C C Encarnação , J F C A Veloso and A L M Silva

Physics Department, Institute for Nanostructures, Nanomodelling and Nanofabrication, University of Aveiro, Aveiro, Portugal

* Author to whom any correspondence should be addressed.

E-mail: anacatarinamagalhaes@ua.pt

Keywords: proton therapy, EasyPET.3D, PMMA phantom, GATE simulation, beam quality control

Abstract

In proton therapy, a conformal and precise radiation dose is delivered to tumors, resulting in improved treatment outcomes and higher survival rates. However, the depth-dose profile (Bragg Peak) poses a significant concern for clinical applications, as even minor spatial uncertainties can lead to undesired doses in normal tissues. Imaging techniques like Positron Emission Tomography (PET) have been proposed to address this challenge. This study evaluates the suitability of the easyPET.3D system for assessing 3D proton beam profiles through Monte Carlo simulations. The primary focus is on accurately predicting the distribution of β^+ emitters produced in a phantom after proton beam irradiation. Simulations were performed to model the irradiation of homogeneous and heterogeneous phantoms with monoenergetic protons (energies ranging from 80 to 160 MeV) and obtain the corresponding PET images of the phantom's irradiation. The β^+ production map (ground truth) generated in the phantoms showed reproducible agreement with the PET image obtained. For the energy beams simulated in this study, the relative deviation between the ground truth image and the PET 3D image was less than 14%, for every beam energy. The easyPET.3D system could also differentiate between the two materials in the heterogeneous phantom. Additionally, the distance between the Bragg peak and the maximum intensity of PET image profile obtained remained constant across all simulated proton energy beams, around 11.7 mm. This suggests that the easyPET.3D system can be used as an effective tool to assess beam quality in proton therapy by measuring the β^+ activation map generated in phantoms and correlate it with the beam's profile.

1. Introduction

Particle therapy using protons or heavier ions stands as a cutting-edge technique of radiotherapy and holds great potential for notable progress in both cancer treatment and research. Its effectiveness derives mainly from the characteristic depth-dose curve, also known as Bragg Curve. Charged particles initially deposit a small amount of energy (plateau), but their energy loss per unit of distance increases with depth [1]. This leads to a prominent peak, known as Bragg peak, when they approach the end of their range within the tissue. This enables the delivery of a high radiation dose to the tumor while preserving the surrounding tissues [2], reducing the total energy deposited in the patient [3].

However, it is still not possible to take full advantage of the potential of proton therapy due to various sources of uncertainty related to the precise location of the distal dose peak. These uncertainties arise from factors such as organ motion, dose calculation approximations, anatomical variations, and biologic considerations, such as miscalculated relative biological effectiveness (RBE) [3]. Such uncertainties can result in clinically significant overdosing of healthy tissues and underdosing of the tumor volume. Consequently, substantial safety margins need to be incorporated into treatments. For instance, current treatment plans implement an approximately 3% uncertainty in dose delivery and a 3 mm uncertainty in the delivery point [2]. In more specific cases, such as brain tumors, the uncertainties are 1.7% + 2 mm, and for prostate and lung cancers, they are 2.0% + 2 mm [4]. Therefore, while clinical range margins address patient-specific uncertainties, additional

© 2025 The Author(s). Published by IOP Publishing Ltd

tools for proton beam monitoring and range verification in phantoms can still be valuable. This study contributes to increasing confidence in the characterization of the beam, which may support quality assurance procedures, and, in the longer term, help maximize the effectiveness and safety of proton therapy.

Multiple experimental approaches for quality assurance of proton beams have been reported [5–11]. However, these measurements are typically conducted using either film dosimetry or ionization chambers, which offer two-dimensional (2D) dose distribution information with limited resolution. Ionization chamber array-based devices such as MatriXX and Zebra (IBA Dosimetry, Germany[1]) is widely used for lateral and depth-dose measurements, respectively, but neither provides three-dimensional (3D) dose information. Film dosimetry, including EBT3 films, can suffer from pixel dispersion that introduces statistical fluctuations in dose readings, affecting precision in regions with highly localized dose variations [10]. Moreover, both ion chamber and film-based methods require frequent recalibration and the fabrication and readout process can be time consuming [11]. An alternative approach is polymer gel dosimetry, which enables 3D dose measurements with high spatial resolution due to its water-equivalent composition that mimics human tissue response [12]. However, they require careful preparation, are prone to contamination, and exhibit time-dependent polymerization as well as LET-dependent dose response, which can lead to dose underestimation in regions such as the Bragg peak, thereby limiting their practicality for routine quality assurance [13].

Among the available imaging techniques, Positron Emission Tomography (PET) is a noninvasive method used for monitoring the proton range [14–17]. PET measures and images the β^+ activity generated by β^+-emitting isotopes (such as ^{11}C and ^{15}O [18]) produced by nuclear interactions along the proton beam path within the patient's tissue [19]. Using PET scanners, it is possible to obtain three-dimensional (3D) distribution maps of the activity of these β^+ emitters [15, 20]. Both the dose and the distribution of β^+ emitter activity vary depending on the ion species, energy, and tissue composition. The PET signal diminishes at the Bragg peak, once the proton energy falls below the energy required for the nonelastic reactions that produce β^+-emitting isotopes [21]. This results in a shift between the fall-off positions of the β^+ activity and the dose distributions [6]. However, effective range verification can still be achieved by comparing the distribution of β^+ emitters measured by PET scanners with the predicted yield from simulations [16]. These simulations must incorporate the timeline of data acquisition and the specific detector response [6]. Consequently, changes in the particle beam range, a critical parameter for treatment quality assurance, can be measured [2].

The integration of PET systems into the clinical environment presents some challenges due to geometric constraints ranging from the high background radiation during beam delivery, low sensitivity of PET imaging, and biological wash-out, which affects directly the activity distribution of the PET imaging [6]. According to [22], proton therapy quality assurance could be improved by incorporating 3D dose measurements mounted on the beam nozzle. These 3D systems could capture the complex distribution of protons, providing detailed information to verify that the range and dose precisely matches the planned treatment volume, thereby reducing uncertainties in treatment delivery.

In this work, simulations were conducted to evaluate the potential performance of the easyPET.3D system [23], a compact, benchtop, and high-resolution PET system to predict the distribution of β^+ emitters in both homogeneous and heterogeneous phantoms, irradiated with proton beams and to assess the quality of the PET signal near the Bragg peak region. A further aim is to investigate the relationship between the β^+ emitter distributions and the proton range, while also providing an independent perspective on beam performance within a single experimental setup.

The following sections present the design, features, and working principles of the easyPET.3D system as well as detailed descriptions of the simulation performed. In this work a detailed comparison of the obtained PET image with the ground truth of the β^+ emitter distribution maps is presented and discussed.

2. EasyPET.3D concept

In contrast to conventional PET scanners, which have detectors distributed uniformly in a full circumference (ring geometry), the easyPET scanners family, developed and patented at the University of Aveiro [24], stands out by its unique acquisition method. It employs only two opposite detector modules that rotate intelligently through a dual motor system with two degrees of freedom, enabling complete coverage of the Field-of-View (FOV) and producing images comparable to those generated by a ring-based PET scanners. Its particular design allowed for a significant reduction in cost compared to traditional full-ring PET detectors. More detailed information about the easyPET.3D movements can be found in [23].

Regarding the detectors, the easyPET.3D system is composed by LYSO:Ce (Cerium-doped Lutetium Yttrium Orthosilicate) crystals, from Epic-Cristal,[2] with dimensions $2 \times 2 \times 30$ mm^3. The system has two crystal matrices, one on each side (32×2 detectors),

[1] https://www.iba-dosimetry.com/proton-therapy/

[2] https://www.epic-crystal.com

Table 1. Specifications of the easyPET.3D system [23].

Specifications	
Weight	20 kg
Total system size	$35 \times 36 \times 38$ cm^3
Transverse FOV	10–48 mm
Axial FOV	73 mm
Coincidence time window	15–40 ns
Used frame duration	100 s
Spatial resolution	0.81 mm^3 (FOV center)
Sensitivity	0.23% (A-FOV centered)
Energy resolution	$11.5 \pm 2.4\%$ @ 511 keV

resulting in a total of 128 detectors positioned face-to-face during the acquisition. On each matrix, crystals are aligned and separated by a reflective paint ($BaSO_4$) with roughly 280 μm of material, to avoid optical cross-talk. For light detection, the state-of-the-art Silicon Photomultipliers (SiPMs) from Hamamatsu[3] S13365-1350PE were used, featuring a 1.3×1.3 mm^2 photosensitive area and 50 μm of pixel width. To facilitate a one-to-one coupling between the SiPMs and the crystals, an optical grease was used.

The unique acquisition method and geometrical position of the detectors in the easyPET.3D system, always face-to-face, allowing to reduce significantly the parallax effect [25].

One of the major advantages of this system is its portability (only weighing about 20 kg), which facilitates the installation in different medical and research environments, like proton therapy centers. In addition, the system achieves a spatial resolution of less than 1 mm, according to NEMA standards [23], enabled by the fine and precise scanning movements, and high density of scanned lines-of-response, allowing high-quality images produced by a custom-made image reconstruction framework, GPU accelerated [26]. These main specifications are represented in table 1, as well as information about the energy resolution and sensitivity of the system. Further details on the system's characteristics can be found in [23].

3. GATE simulations

GATE[4] (a Geant4-based code) enables the modeling of various aspects of emission tomography and radiation therapy, including geometry, physics involved in the interaction of radiation with matter, movements, radiation detection, data output, etc. Users can interactively assemble these components according to their requirements using a programming language and write a macro file [27, 28]. In this study, GATE version 9.2, using Geant4 version 11.0.3, was used.

GATE was used to simulate the irradiation of phantoms as well as the acquisition of PET images.

[3] https://www.hamamatsu.com/jp/en.html
[4] http://www.opengatecollaboration.org/

Designing and optimizing new PET scanner systems for proton range monitoring presents specific challenges. This process involves simulating proton beam delivery to the phantom, producing β^+-emitting isotopes, and simulating 511 keV gamma transport to the PET detectors to record coincidence events for subsequent PET image reconstruction [29]. These processes are associated with uncertainties, mainly regarding the nuclear model used. However, according to [29, 30] the validation of Monte Carlo simulations was subject of extensive research and as so with the correct tunning of the physics these uncertainties are not expected to compromise the validity of the results.

Performing all these tasks in a single-stage Monte Carlo (MC) simulation is not ideal, as it requires time-consuming tracking of many particles and their interactions.

To simplify the process and manage simulation capacity, the simulation was divided into two stages. The first stage reproduces the irradiation of a phantom by a proton pencil beam. The second stage involves acquiring a PET image of this irradiation (figure 1).

The block diagram in figure 1 illustrates the structure of the simulation. In Stage 1, part (a) shows the inputs for the proton beam irradiation of a phantom, including the simulation scheme. Part (b) shows the output of this stage–a 3D image of the distribution of β^+-emitting isotopes generated. Stage 2 (PET image acquisition), part (c) uses the 3D image obtained from Stage 1 as an input. This results in part (d), a raw file containing all the singles registered by the easyPET detectors. Then, the file is filtered in part (e) and reconstructed in part (f) to obtain the final PET image of the phantom irradiation.

3.1. First simulation stage setup - proton beam irradiation

A visual description of the phantoms irradiation by proton beams with different energies are shown in figure 1(a). It can be seen that the beam propagates along the z-axis and the beam profile was assumed to be a Gaussian distribution with standard deviations σ_x and σ_y of 3 mm in the isocenter position [31]. The intrinsic beam divergence simulated was $\sigma = 3$ mrad, negligible compared to the effect of multiple Coulomb scattering [32].

In terms of beam energy, monoenergetic beams of 80, 100, 120, 140, and 160 MeV were simulated for the homogeneous phantom, whereas the heterogeneous phantom was irradiated with a 95 MeV beam. These beams generated a Gaussian energy spectrum, and the standard deviation from the target proton energy was defined as 1 %. A total of 3×10^9 proton primaries were generated, and the total time of irradiation was 1 s, to minimize the simulation time while ensuring sufficient statistical information.

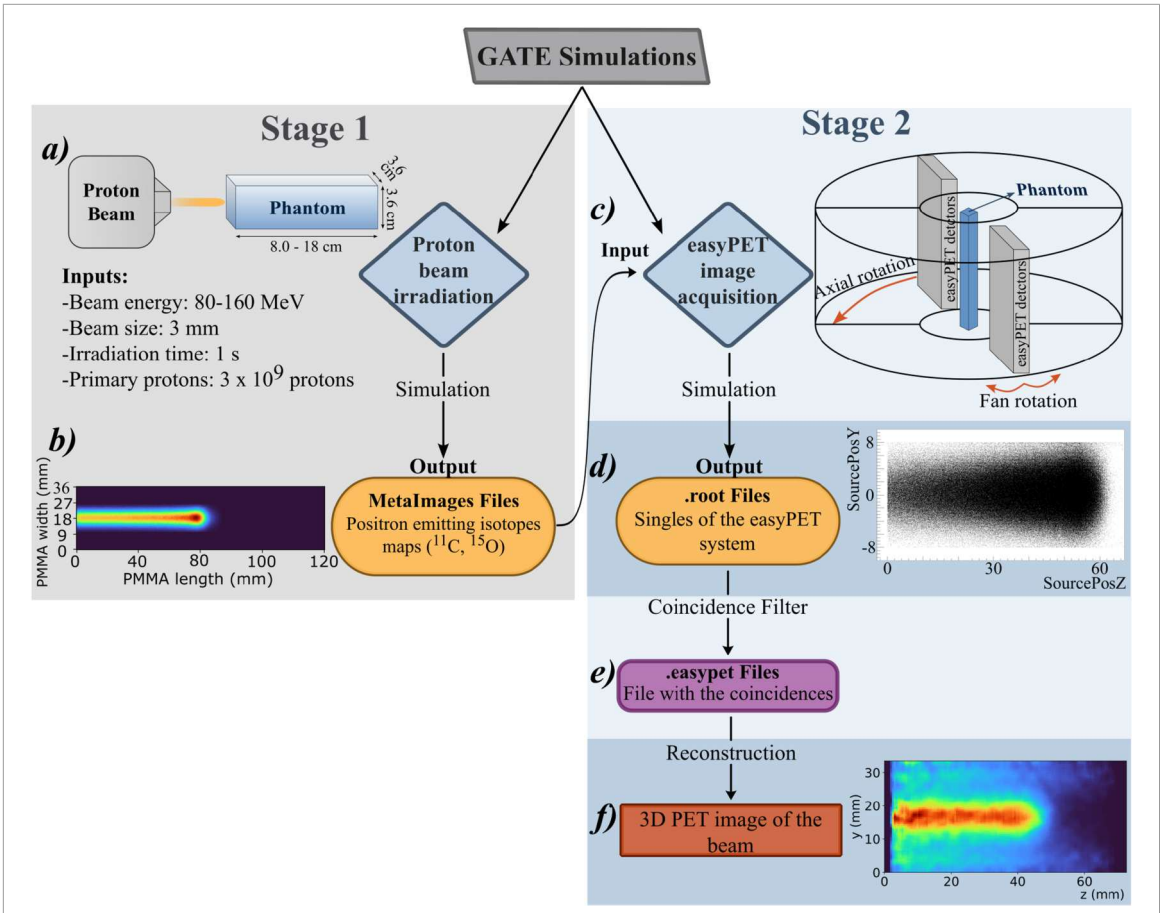


Figure 1. Block diagram of the GATE simulations performed. The first stage (on the left) includes (a) proton irradiation of the phantom and the corresponding (b) 3D map output (ground truth). The second stage (on the right) uses (c) the 3D maps obtained in the first stage as a source for the PET image acquisition simulation. (d) Raw data obtained from the second stage simulation is then (e) filtered and organized to be reconstructed by the reconstruction algorithm, resulting in the final PET image of the phantom irradiation by a proton beam (f).

The physics list employed in the first simulation stage was QSP_BIC_HP_EMY, which incorporates the Binary Cascade (QGSP_BIC) for modeling hadronic interactions, a high precision library of neutron interactions (HP) below 20 MeV and the electromagnetic physics component in option 3 (EMY) [29].

The main goal of this stage is to obtain production maps of β^+-emitting radioisotopes, which will later be considered the ground truth images. Here, the *ProductionAndStoppingActor* was attached to the phantom to store the distribution of the β^+-emitters isotopes to be used in further simulation steps. The radioisotopes stored were the ones with the longest half-life and largest contribution to β^+ emission images, ^{11}C and ^{15}O [21]. These 3D maps were stored in *MetaImage* files with a simplified header containing basic information about the matrix size, voxel size, and number of voxels. Posteriorly, these maps (ground truth) were used as source for PET imaging acquisition simulation.

3.2. Second stage simulation setup - easyPET.3D image acquisition

During the second simulation stage, the PET image of the β^+-emitters activated in the phantom during beam irradiation was generated to be compared with the ground truth image (3D β^+-emitters maps stored and obtained in the 1st simulation stage). Figure 1(c) shows a summary schematic of the model developed in this stage, including the phantom position and the two different rotation movements of the PET system.

3.2.1. Geometry and detectors movement

The geometry system was modeled as described in section 2. It consists of two blocks of detectors (a total of 128 detectors), separated by 6 cm, each block containing the LYSO crystals.

Two macro files were created to describe the detector's movements. These files contain the positions and rotation angles of the detector's modules at each instant, necessary to simulate the movements of the axial and fan motors. Figure 2 demonstrates the two types of movements (axial and fan) performed by the easyPET.3D system. For each position of the axial motor, the fan motor executes a fan movement (several positions with an angular step of about 0.9°) to cover all the FOV. These motor positions vary with five parameters: total number of turns, acquisition time per position, fan step angle, fan aperture, and axial step angle. For the study presented here,

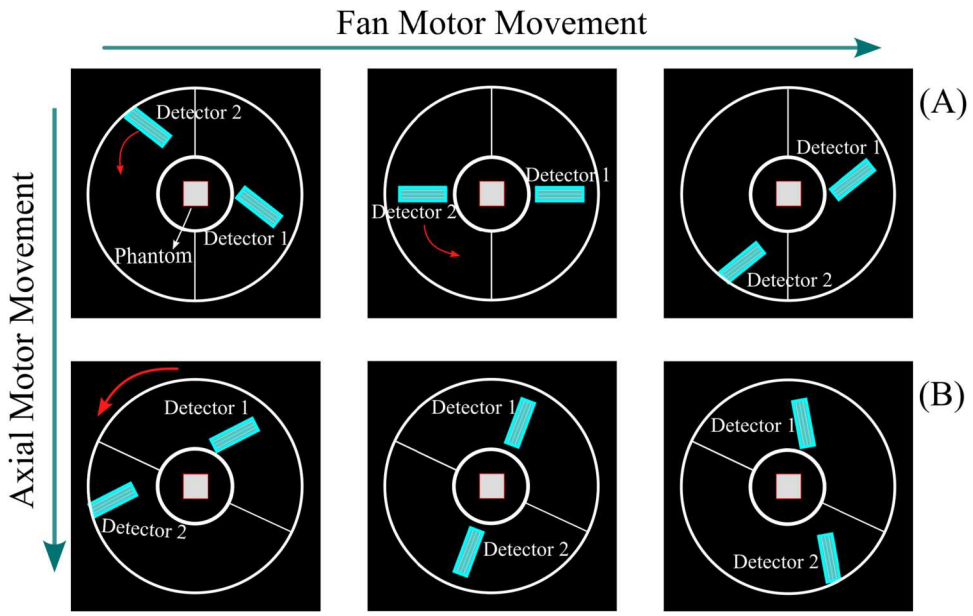


Figure 2. Representation of the detector's movement around the PMMA phantom simulated in GATE. The PMMA phantom is depicted in the figure as a white square in the center. In the first row (A), the axial motor is in a fixed position, while in the second row (B), the axial motor changes position. Along both rows, it is shown the fan motor movement (fan movement).

the parameters used are represented in table 2. With these parameters, the resultant FOV is 33.5 × 33.5 × 72.68 mm^3 and the acquisition time is around 300 s.

3.2.2. Physics list

The simulations at this stage were performed using *emstandard_opt1* list of physics processes. To complement the physics list, *Decay* and *RadioactiveDecay* processes were included.

3.2.3. Source

A voxelized source was used to define the simulation source. In this way, it was possible to use the 3D maps obtained from the previous stage of the simulations (*MetaImage* of the isotopes distribution maps) and convert it into a true isotope activity value. For this, the radioisotope half-life time ^{11}C and ^{15}O were considered.

3.2.4. Data output

The interactions of particles with the system detectors (singles) were recorded in .root files. The events were organized and filtered to obtain the coincidence events to be used by the dedicated reconstruction algorithm [26], to obtain the final PET image. The algorithm used was Maximum Likelihood Expectation Maximization (MLEM) with 30 iterations and a voxel size of 0.5× 0.5 × 0.568 mm^3 [26]. The number of iterations was chosen in order to provide a balance between image quality and noise, as detailed in [26].

Table 2. Parameters used to define the positions of the motors for the simulation of the PET image.

Parameters	Value
Total number of frames	3
Acquisition time per position	0.005 s
Total acquisition time	300 s
Fan step angle	0.9°
Fan aperture	90°
Axial step angle	1.8°

3.3. Phantoms

Two different phantoms were used in this study: one homogeneous (figure 3(A)) and other heterogeneous, composed by two distinct materials (figure 3(B)).

The material used for the homogeneous phantom was PMMA (from *GATEMaterials.db*) with a density of 1.195 g cm^{-3}. Table 3 provides detailed information on the density and chemical composition of the materials used in this study. The homogeneous phantom model is shown in figure 3(A), with a fixed lateral size of 3.6 × 3.6 cm^2. The longitudinal size of the phantom varied according to the beam energy, ranging from 8.0 cm for the lowest energy to 18 cm for the highest energy. Higher energies require larger phantoms to fully stop the beam, and for each energy the phantom was dimensioned so that the distal region containing the Bragg peak was located within the final 7.3 cm of the phantom and entirely inside the scanner's axial FOV.

The heterogeneous phantom consists of four PMMA slices and three slices of muscle-equivalent tissue (as detailed in table 3), arranged alternately along the beam direction, with dimensions of 3.6 × 3.6 × 7.3 cm^3.

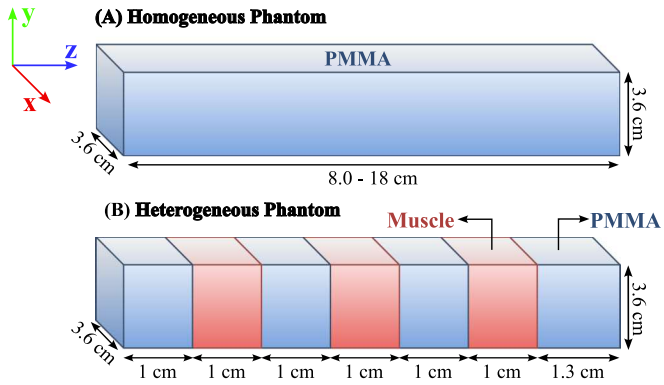


Figure 3. (A) Homogeneous PMMA phantom and (B) Heterogeneous phantom, where the blue slices represent PMMA and the red slices represent Muscle-equivalent tissue.

Table 3. Density and chemical composition (fraction) of the materials used for the phantoms.

Material	ρ (g cm^{-3})	H (%)	C (%)	O (%)	Others (%)
PMMA	1.19	8.05	59.99	31.96	—
Muscle	1.05	10.20	14.30	71.00	4.5

4. Results and discussion

The results section is divided into three subsections. The first section details the results from the 1st stage of the simulation, which involves proton beam irradiation. In this section, the ground truth images corresponding to the β^+ activity maps as well as the dose distribution maps are displayed. The 2nd section presents the results from the subsequent simulation stage, focusing on the PET image acquisition. The 3D images obtained for various energies are shown, analyzed, and compared with the ground truth images. Finally, the relationship between the dose distribution maps and the PET images is extrapolated and discussed.

4.1. Proton beam irradiation

Figures 4(A) and (B) present the depth dose profile and the corresponding β^+-emitting production map for monoenergetic proton beams in a PMMA phantom. The dose and β^+ activity-induced maps depict five different energy values ranging from 80 to 160 MeV. In all these maps, the horizontal axis represents the penetration depth of the beam (in mm), while the vertical axis shows the lateral dispersion of the beam (in mm). The color in the dose maps (figure 4(A)) represents the absorbed dose per voxel (in Gy), and in the β^+ activity maps (figure 4(B)), it indicates the number of β^+ emitter isotopes produced per voxel.

Posteriorly, the β^+-emitting production maps were used in the second stage as the data source, making these images (figure 4(B)) the ground truth for further analysis.

In both the dose and β^+-emitting production maps, greater dispersion of the particles is visible along the vertical axis for higher energies, as well as an increase of the particle's path length along the horizontal axis. These effects are illustrated in figure 4, which also includes the 1D line profiles of the dose (C) and the β^+ activity distribution (D) for the different energy values, showing the influence of the incident protons energy when interacting with the phantom.

As the beam energy increases, the dose distribution changes, leading to a lower and broader Bragg peak, along with a shift of all curves, indicating deeper proton beam penetration into the material.

In terms of the β^+ activity line profile shape (figure 4(D)), a sharp decline in positron concentration near the Bragg Peak is observed, which is consistent with the theoretical model, as nuclear reactions are more likely to occur at higher proton energies. This is primarily influenced by the energy thresholds of 16.6 MeV and 20.3 MeV for the most relevant fragmentation reactions, leading to the production of ^{15}O and ^{11}C, respectively [33]. As a result, most of the β^+-activity stops before the Bragg peak. However, some ^{11}C and ^{15}O nuclei are still produced by secondary particles, such as protons and neutrons, causing a small but visible contribution in the declining slope part of the β^+-emitting production map [34].

The β^+-emitting production map shape near the Bragg Peak could differ across various materials, based on the proton residual range at energies below the reaction thresholds and the O/C ratio in the material composition [33]. Knowing the material composition allow us to infer a systematic relationship between the position of the Bragg peak and the peak of the β^+-emitting production map. This distance is primarily determined by the proton rest range as they fall

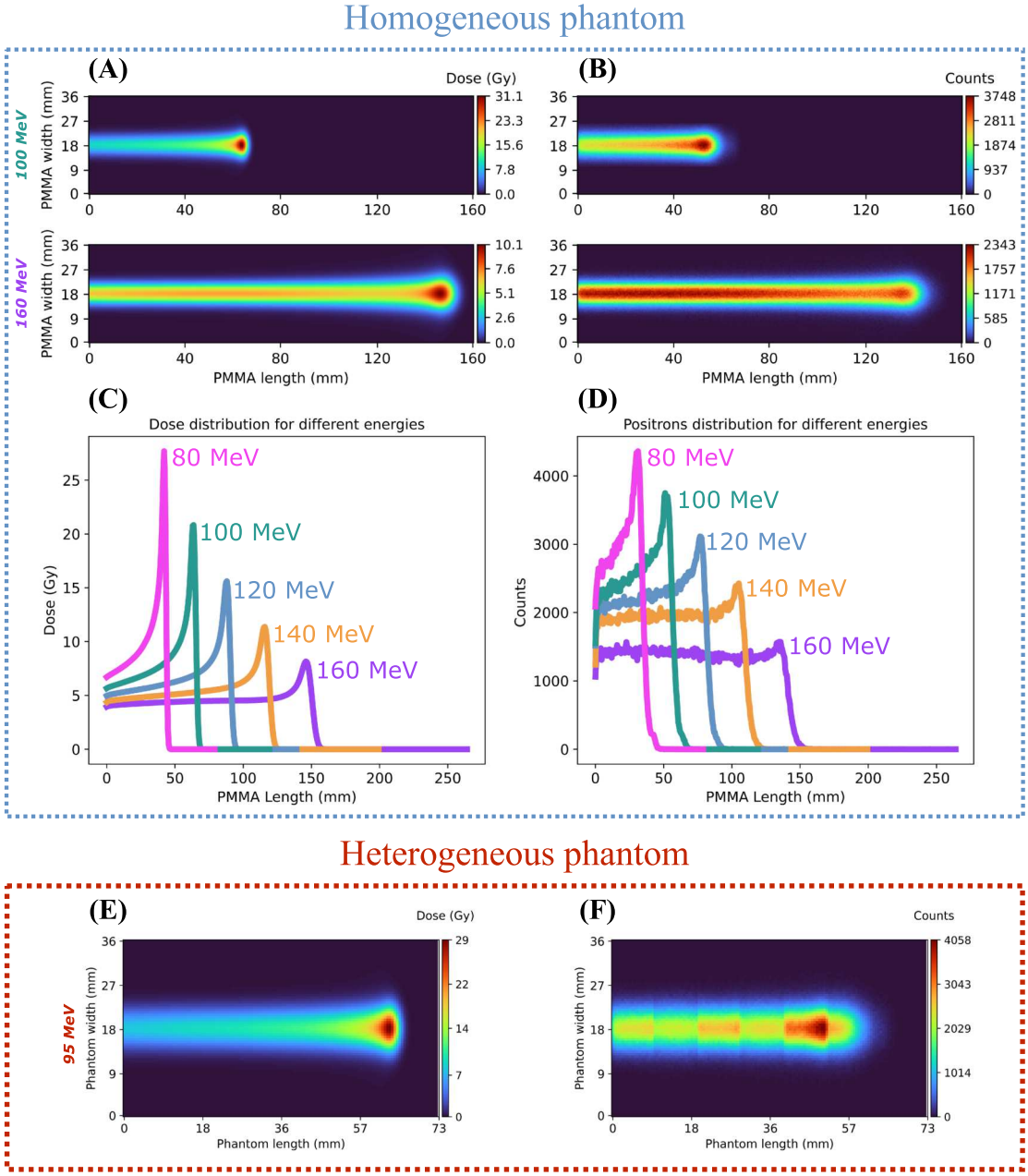


Figure 4. Depth dose profile (A) and β^+ activity distribution maps (central voxel) (B) of homogeneous PMMA phantom when irradiated with proton beams with an energy of 100 and 160 MeV. Respective 1D dose distribution profile (C) and 1D β^+ activity profile (D) along the irradiation direction. Depth dose profile (E) and β^+ activity distribution maps (F) of heterogeneous phantom when irradiated with a 95 MeV proton beam.

below the energy thresholds for fragmentation reaction [34].

Regarding the heterogeneous phantom, the depth dose profile and the β^+ activity distribution map for 95 MeV beam irradiation are shown in figures 4(E) and (F), respectively. The β^+ activity distribution map clearly reveals the slices of the heterogeneous phantom, as the two constituent materials differ in both density and composition.

4.2. EasyPET.3D image acquisition

4.2.1. Homogeneous phantom

Using the β^+-emitting production map obtained in the 1st simulation stage, along with the modeling of the easyPET.3D system, and subsequent filtering and reconstruction, we obtained PET images of the phantom irradiation. Figure 5 illustrates multiple images of the homogeneous phantom (for different beam energies) with several transverse planes (XY) along the axial view (YZ), obtained. These images were generated using the dedicated easyPET reconstruction algorithm, in which, for higher beam energy cases, a greater dispersion is evident, as also seen in the ground truth images. This increased dispersion results from a smaller difference between the peak and the baseline in the maps, leading to image deterioration.

Before direct comparison with the PET images, the decay formula was applied to the ground truth to

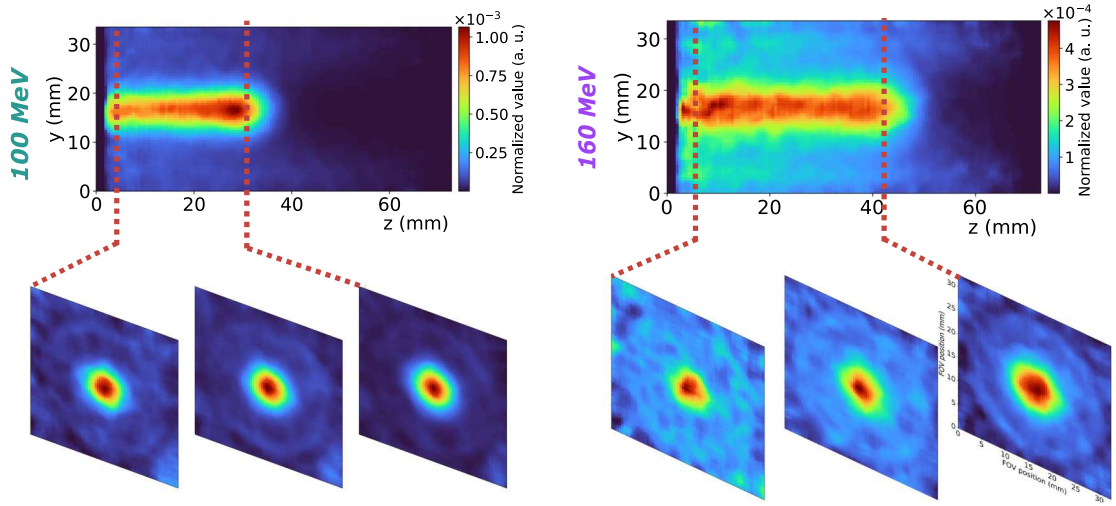


Figure 5. PET images of the homogeneous phantom irradiation, in the transverse and axial planes, for 100 and 160 MeV beams. The images were normalized by the sum of all pixel intensities.

determine the maps with the number of β^+ particles that could effectively be produced during the PET acquisition time (300 s). Then, comparing these PET images with the ground truth maps confirms that the PET images closely match with the ground truth distribution (figures 6(A) and (B)). Figures 6(A) and (B) shows the relative deviation between the projections in the × and z direction, respectively, of the β^+-emitting production map and the PET image. These maps reveal only minor differences between the ground truth and PET image projections, as evidenced by the predominance of dark blue regions in the relative deviation maps for both the axial and transverse planes. The specific case illustrated in figure 6 (120 MeV), the median deviation values are 3.6 % in the axial plane and 7.0 % in the transverse plane.

Since the easyPET.3D system successfully produced a 3D PET image of the beam irradiation, a more detailed analysis was conducted in 3D. The relative deviation was calculated voxel by voxel between the 3D ground truth and the 3D PET image. Figure 7 presents the 3D distribution of relative deviation values across the various simulated energies. The highest median deviation value, recorded as 14.5 %, occurs with an incident beam energy of 120 MeV (case represented in figure 6). For the other energies, this value varies between 5.2 % and 12.7 %, with smaller values observed at higher energies, confirming the capability of easyPET.3D to image the irradiation of the phantom.

In figure 6(C), it is evident that the shape of the 1D profiles of the PET image closely matches the 1D β^+ activity profile (ground truth profile). Furthermore, the figure confirms that when the proton energy drops below the fragmentation reaction energy thresholds, the production of β^+-emitting nuclides diminishes. This demonstrates that the easyPET.3D system has the potential to extract information about the proton's path through the phantom.

4.2.2. Heterogeneous phantom

Figure 8(A) shows the activity profiles along the z-axis of the heterogeneous phantom, with all images normalized to the sum for comparison. It is evident that, unlike the uniform profiles seen in homogeneous phantoms, the heterogeneous phantom displays distinct regimes in activity. This indicates that the easyPET.3D system can clearly differentiate between regions made of different materials.

The reduced activity in the muscle slices compared to the PMMA slices is primarily attributed to the lower carbon content in the muscle material (as detailed in table 3) and the specific time window selected for measurement (300 s). Due to the shorter half-life of ^{15}O, most of the oxygen activity decays quickly, making the longer-lived ^{11}C the dominant contributor during this period. Figure 8(B) shows the 1D projection of the β^+ activity profile and the PET profile for the irradiation of the heterogeneous phantom. In this figure, the slices corresponding to the two different materials are clearly visible. Three activity deficits, each approximately 10 mm wide, can be observed at around 10 mm, 30 mm, and 50 mm from the phantom's entrance, corresponding to the actual positions of the muscle slices. This comparison highlights that in the heterogeneous phantom, the regions corresponding to the PMMA slices align closely with the 1D projection curve of the homogeneous phantom. Additionally, the maximum intensity of the homogeneous β^+ activity profile appears earlier than that of the heterogeneous curve. This delay occurs because the muscle slices, having a lower density, require more material to fully stop the beam in the heterogeneous phantom.

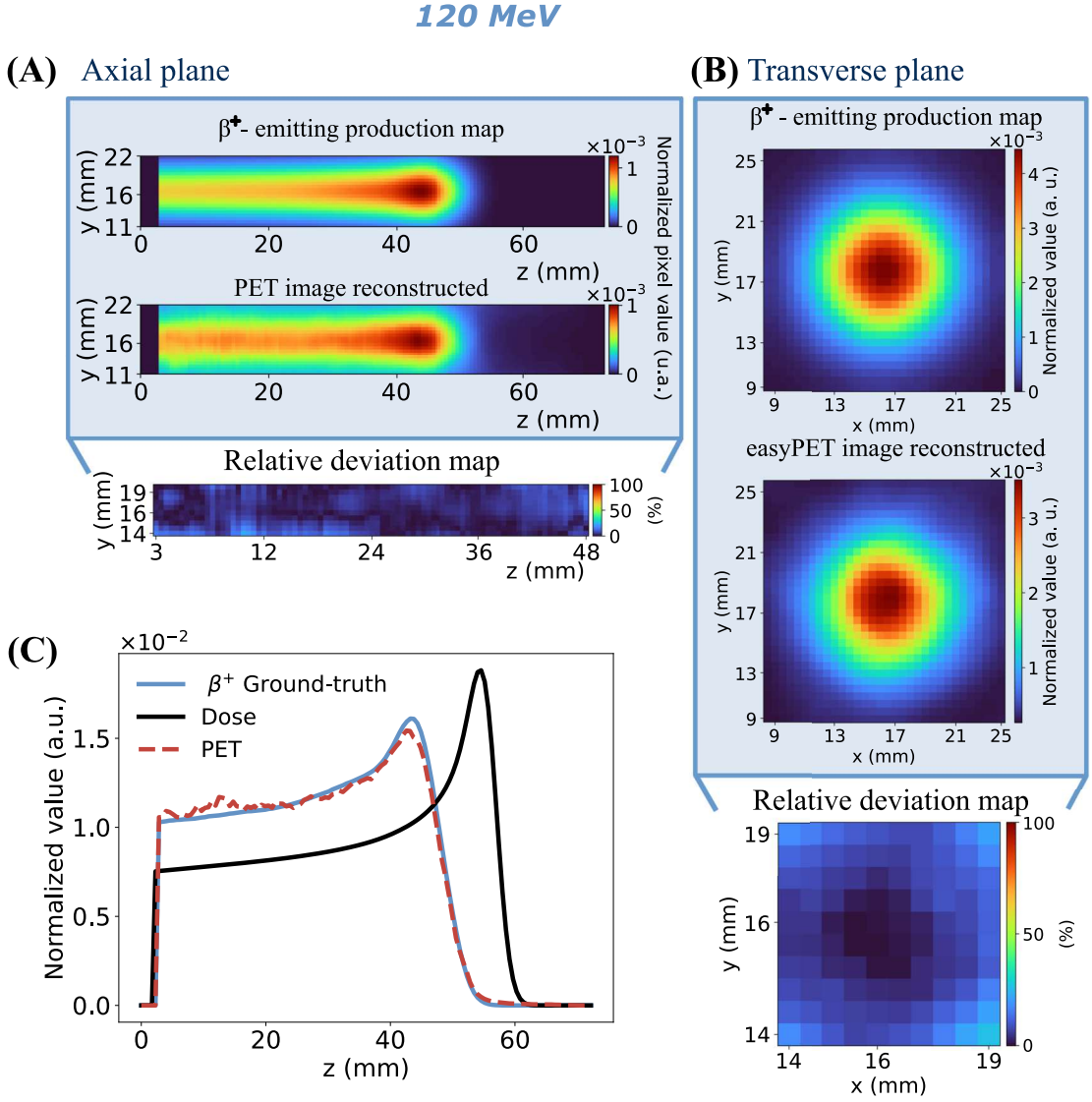


Figure 6. (A) Relative deviation between the ground truth map of the homogeneous phantom generated and the PET image obtained, in the axial plane (YZ). (B) Transverse view (XY) of the β^+-emitting map distribution near the maximum intensity and the PET image in the same position. The relative deviation between the ground truth map generated and the PET image in the transverse plane is also shown here. (C) Comparison of the 1D projection of the β^+ activity profile and the PET profile in the axial plane.

4.3. Correlation between dose maps and PET images

To extract some correlation between the dose maps and the PET images, Gaussian and sigmoid curves were adjusted to the 1D dose profile and the 1D PET profile. The peak values and the 50% peak fall-off values were extracted from these fitted curves. Table 4 lists the distance between the Bragg peak position and the maximum intensity of the PET image position and the distance between the Bragg Peak position and the 50% distal fall-off position of the PET profile for different values of beam energy. The errors presented in table 4 were calculated using the covariance matrix obtained from the Gaussian and sigmoid fits, with error propagation applied during the subtraction of the two positions.

Analysis of table 4 reveals that the distance between the Bragg peak and the PET peak remains consistent across different beam energies. However, the distance between the Bragg peak and the 50% fall-off of the PET profile decreases as the beam energy increases. This trend is illustrated in figure 9, which includes the different relation points from the β^+ activity distribution curve and the dose distribution curve under analysis. The trend of the obtained values is consistent with previously reported findings in the literature [33, 34].

As the proton energy increases, the distance between the Bragg peak and the PET peak remains nearly constant. This is evident in figure 9(A) and confirmed by the linear fit, which shows a slope of 0.0025 mm MeV^{-1}, closely matching the slope of the ground truth linear fit (0.0020 mm MeV^{-1}). This occurs because the β^+ depth profile and the location of the Bragg peak are primarily determined by the remaining range of the protons when they fall below the nuclear reaction energy threshold [33, 34], an effect verified in the PET images. In contrast, at higher

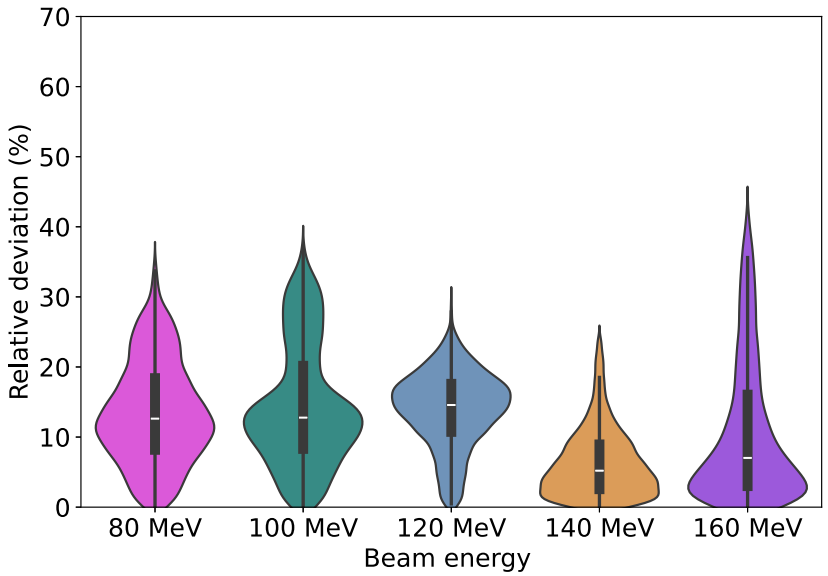


Figure 7. Violin plot with the distribution of the relative deviation (%) values of all voxels (3D) for different beam energies.

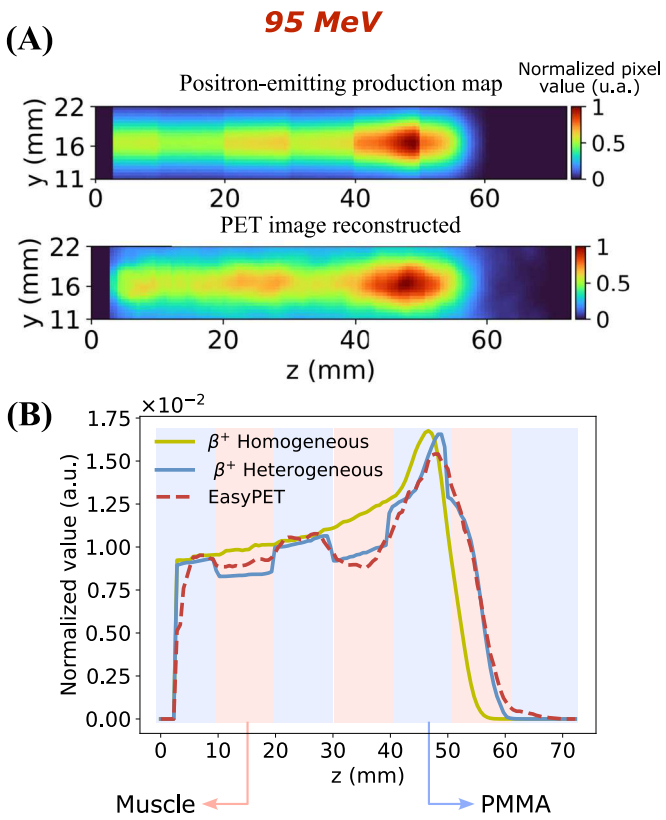


Figure 8. (A) Ground truth map of the heterogeneous phantom generated and the PET image obtained. (B) Comparison of the 1D β^+ activity profile and the 1D PET profile.

proton energies, the 50% peak falloff in the PET profile occurs closer to the Bragg peak, as shown by the negative slope of the points in figure 9(B), which is consistent with results reported by [33]. It is crucial to consider these effects when attempting to establish a correlation between dose deposition and PET images for dose distribution verification. According to the data collected and presented in this paper, the easyPET.3D system shows great promise in predicting the dose peak.

As this study focused on homogeneous and simple heterogeneous phantoms, future research will explore more complex heterogeneous phantoms and additional beam configurations, such as the use of spread-out Bragg peaks. Moreover, future efforts will focus on studying the system in situ at a proton therapy

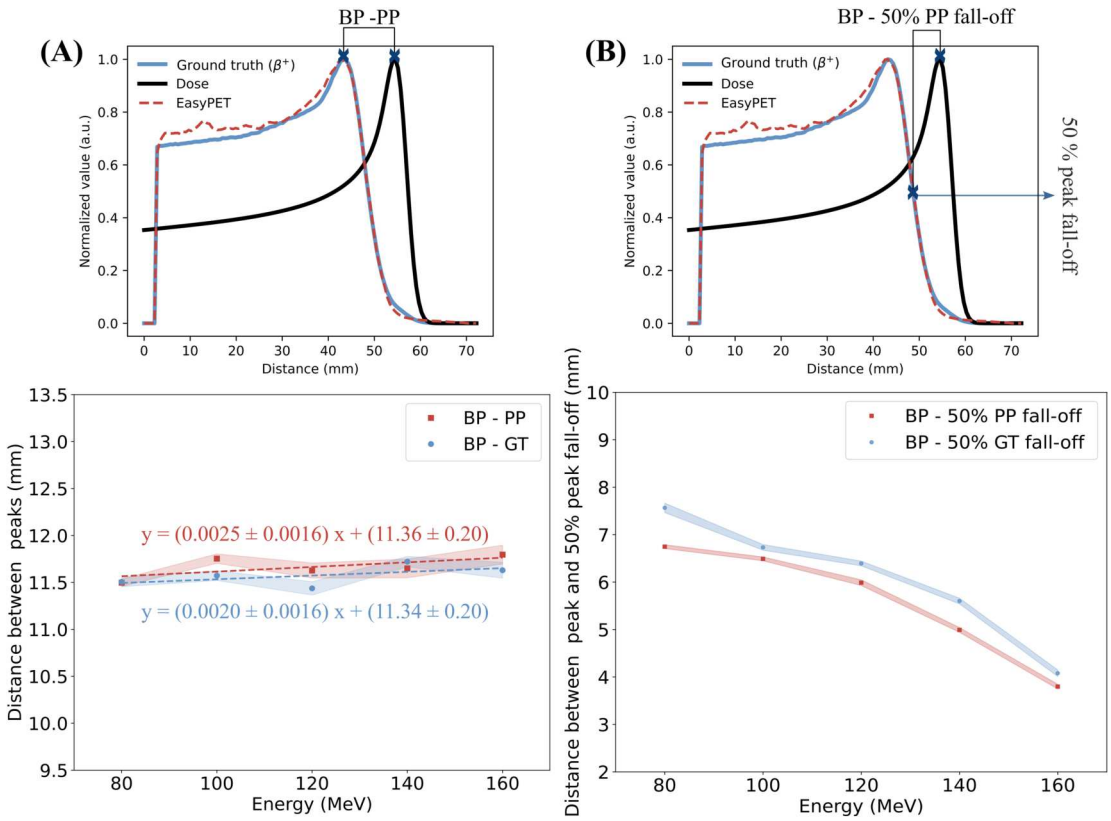


Figure 9. Graphic representation of the (A) distance between the Bragg peak and the maximum intensity of both the PET (PP) image and the ground-truth (GT), and (B) the distance of the Bragg peak and the 50 % peak fall-off of the PET profile (50 % PP fall-off) and 50 % peak fall-off of the ground truth profile (50 % GT fall-off).

Table 4. Distance between the Bragg peak (BP) and the maximum intensity of PET profile (PP), and distance between the Bragg peak (BP) and the 50% peak falloff in PET (50% PP falloff) profile.

Energy (MeV)	BP - PP (mm)	BP–50% PP falloff (mm)
80	11.50 ± 0.04	6.75 ± 0.04
100	11.75 ± 0.05	6.49 ± 0.04
120	11.63 ± 0.08	5.99 ± 0.06
140	11.65 ± 0.10	4.99 ± 0.05
160	11.80 ± 0.10	3.80 ± 0.05

center to validate the simulation results and on developing tools to enhance its efficacy in quality assurance for proton therapy.

5. Conclusion

The feasibility of using the easyPET.3D system for monitoring proton therapy was evaluated, using the Monte Carlo simulations. This study modeled the irradiation of homogeneous and heterogeneous phantoms and the scanning of the dedicated PET system. Images were generated demonstrating a capable imaging performance, with an average deviation of 10 % from the ground truth images.

In terms of count rate performance, our study indicates that the activity signal generated by the beam parameters conventionally used in proton therapy centers is enough to be detected by the easyPET.3D system.

The present study demonstrates that the difference between the position of the maximum intensity in the easyPET.3D image and the Bragg peak position, remains consistent as the proton beam energy increases, as indicated by the linear fit with a slope close to zero. The distance between these two maxima remains constant as the proton beam energy increases. However, the 50% distal fall-off position of the easyPET.3D curve moves closer to the Bragg peak position at higher proton beam energies. These results confirm that the images produced by the easyPET.3D system are consistent with effects described in the literature. This finding suggests that, in the long term, the easyPET.3D system could contribute to enhancing quality assurance in proton therapy.

Additionally, the easyPET.3D system successfully distinguished between the two materials in the heterogeneous phantom, reinforcing its potential for assessing proton beam quality using more complex phantoms.

Furthermore, the system compactness is beneficial for an easier installation in proton therapy centers and enabling an in-room installation. This could be a great option to accelerate the image acquisition process immediately after phantom irradiation and consequently, proton beam quality control used in the proton therapy center. Additionally, the easyPET.3D configuration

features a significantly smaller footprint, with a noticeably smaller size, lower weight, and reduced cost compared to other existing PET systems.

Beyond its application in quality assurance, it is worth noting that the easyPET.3D system was originally developed for small-animal imaging. This opens the possibility of extending the technology toward preclinical *in vivo* applications in the longer term. Such developments could broaden the impact of the system by enabling both quality assurance in proton therapy and preclinical research in molecular imaging.

Acknowledgments

This work was supported by A) project i3N, UIDB/50025/2020, UIDP/50025/2020 and LA/P/0037/2020, financed by national funds through the FCT/MEC; B) project HadronPET.3D- COMPETE2030-FEDER 00755500, funded by FEDER program and by national funds through the FCT, Portugal; and C) grant to A C M Magalhães (PRT/BD/153499/2021) through FCT, Portugal by project https://doi.org/10.54499/PRT/BD/153499/2021.

Data availability statement

All data that support the findings of this study are included within the article (and any supplementary files).

Author contributions

A C M Magalhães 0000-0001-9412-8854
Conceptualization (equal), Data curation (lead), Formal analysis (lead), Investigation (lead), Methodology (lead), Software (lead), Visualization (lead), Writing – original draft (lead), Writing – review & editing (equal)

P M M Correia 0000-0001-7292-7735
Conceptualization (equal), Formal analysis (equal), Supervision (equal), Writing – review & editing (equal)

P M C C Encarnação 0000-0003-4435-4719
Software (equal), Writing – review & editing (equal)

J F C A Veloso 0000-0002-7107-7203
Project administration (supporting), Writing – review & editing (supporting)

A L M Silva 0000-0002-8363-0109
Conceptualization (equal), Formal analysis (equal), Funding acquisition (lead), Project administration (lead), Supervision (lead), Writing – review & editing (equal)

References

[1] Grau C, Durante M, Georg D, Langendijk J A and Weber D C 2020 Particle therapy in europe *Molecular Oncology* **14** 1492–9
[2] Piliero M A *et al* 2016 First results of the inside in-beam pet scanner for the on-line monitoring of particle therapy treatments *18th International Workshop on Radiation Imaging Detectors* **11** C12011
[3] Paganetti H 2012 Range uncertainties in proton therapy and the role of monte carlo simulations *Phys. Med. Biol.* **57** 6
[4] Peters N, Wohlfahrt P, Hofmann C, Möhler C, Menkel S, Tschiche M, Krause M, Troost E G, Enghardt W and Richter C 2022 Reduction of clinical safety margins in proton therapy enabled by the clinical implementation of dual-energy ct for direct stopping-power prediction *Radiother. Oncol.* **166** 71–8
[5] Arjomandy B, Sahoo N, Ciangaru G, Zhu R, Song X and Gillin M 2010 Verification of patient-specific dose distributions in proton therapy using a commercial two-dimensional ion chamber array *Med. Phys.* **37** 5831–7
[6] Knopf A C and Lomax A 2013 *In vivo* proton range verification: a review *Phys. Med. Biol.* **8** 131–60
[7] Lin L, Kang M, Solberg T D, Mertens T, Baumer C, Ainsley C G and McDonough J E 2015 Use of a novel two-dimensional ionization chamber array for pencil beam scanning proton therapy beam quality assurance *Journal of Applied Clinical Medical Physics* **16** 270–6
[8] Ding X, Younkin J E, Shen J, Bues M and Liu W 2021 A critical review of the practices of proton daily quality assurance programs *Therapeutic Radiology and Oncology* **5** 12
[9] Bizzocchi N, Fracchiolla F, Schwarz M and Algranati C 2017 A fast and reliable method for daily quality assurance in spot scanning proton therapy with a compact and inexpensive phantom *Med. Dosim.* **42** 238–46
[10] Carnicer A, Angellier G, Gérard A, Garnier N, Dubois C, Amblard R and Hérault J 2013 Development and validation of radiochromic film dosimetry and monte carlo simulation tools for acquisition of absolute, high-spatial resolution longitudinal dose distributions in ocular proton therapy *Radiat. Meas.* **59** 225–32
[11] Zhou S 2023 *Multi-layer strip ionization chamber for proton quality assurance Ph.D. Dissertation, Washington University*
[12] Zhu L, Du Y, Peng Y, Xiang X and Wang X 2023 End-to-end qa with polymer gel dosimeter for photon beam radiation therapy *Gels* **9**
[13] Yao C-H, Huang E-Y, Juan K-J, Juang P-J, Juan Y-H and Chang Y-J 2023 Feasibility evaluation of n-isopropyl acrylamide 3d gel dosimeters for proton therapy *PLoS One* **18** 1–12
[14] Moglioni M *et al* 2022 In-vivo range verification analysis with in-beam pet data for patients treated with proton therapy at cnao *Frontiers in Oncology* **12** 929949
[15] Zhang J, Lu Y, Hsi W, Zhang J, Sheng Y, Shi L, Wang W, Lu J, Zhou R and Cheng J 2018 Evaluation of proton therapy accuracy using a pmma phantom and pet prediction module *Frontiers in Oncology* **8** 523
[16] Nemallapudi M V, Rahman A, Chen A E-F, Lee S-C, Lin C-H, Chu M-L and Chou C-Y 2022 Positron emitter depth distribution in pmma irradiated with 130-mev protons measured using tof-pet detectors *IEEE Transactions on Radiation and Plasma Medical Sciences* **6** 345–54
[17] Ma Q, Mu D, Zhang R, Liu Z, Wan L, Liu Y, Qiu A, Yang Z and Xie Q 2025 Development and evaluation of an in-beam pet system for proton therapy monitoring *Phys. Med. Biol.* **70**
[18] Rahman A U, Nemallapudi M V, Chou C Y, Lin C H and Lee S C 2022 Direct mapping from pet coincidence data to proton-dose and positron activity using a deep learning approach *Phys. Med. Biol.* **67**
[19] Bisogni M G *et al* Inside in-beam positron emission tomography system for particle range monitoring in hadrontherapy *Journal of Medical Imaging* **4** 011005

[20] Piliero M A, Bisogni M G, Cerello P, Guerra A D, Fiorina E, Liu B, Morrocchi M, Pennazio F, Pirrone G and Wheadon R 2015 Performance of a fast acquisition system for in-beam pet monitoring tested with clinical proton beams *Nuclear Instruments and Methods in Physics Research, Section A: Accelerators, Spectrometers, Detectors and Associated Equipment* **804** 163–6
[21] Beebe-Wang J, Vaska P, Dilmanian F A, Peggs S G and Schlyer D J 2003 Simulation of proton therapy treatment verification via pet imaging of induced positron-emitters *IEEE Nuclear Science Symposium Conference Record* **4** 2496–500
[22] Flanz J, Litzenberg D and Chen H 2016 *Particle Therapy Co-Operative Group (PTCOG) Subcommittee:* https://ptcog.site/images/Docs/White%20Paper%20QA%20Efficiency_Final.pdf
[23] Ribeiro F M, Encarnação P M C C, Silva A L M, Correia P M M, Pinto A X, Castro I F, Santos A C and Veloso J F C A 2025 Sensitivity and spatial resolution optimization of a high-resolution preclinical pet with a unique acquisition method *IEEE Transactions on Radiation and Plasma Medical Sciences* 1–1
[24] Veloso J, Castro I, Moutinho L, Carramate L, Correia P and Silva A 2016 Positron emission tomography sistem and method with two rotation shafts WO2016147130A10
[25] Arosio V, Caccia M, Castro I F, Correia P M, Mattone C, Moutinho L M, Santoro R, Silva A L and Veloso J F 2016 easypet: a novel concept for an affordable tomographic system *Nuclear Instruments and Methods in Physics Research A* **845** 644–7
[26] Encarnação P, Correia P, Silva A L M, Ribeiro F M, Castro I F and Veloso J F C A 2025 A modified orthogonal-distance ray-tracer method applied to dual rotation pet systems *Physics in Medicine & Biology* **70**
[27] Sarrut D *et al* 2022 The opengate ecosystem for monte carlo simulation in medical physics *Phys. Med. Biol.* **67** 184001
[28] Sarrut D *et al* 2021 Advanced monte carlo simulations of emission tomography imaging systems with gate *Phys. Med. Biol.* **66** 5
[29] Borys D *et al* 2022 Protheramon—a gate simulation framework for proton therapy range monitoring using pet imaging *Phys. Med. Biol.* **67** 224002
[30] Kraan A C 2015 Range verification methods in particle therapy: Underlying physics and monte carlo modelling *Frontiers in Oncology* **5** 139363
[31] Pedroni E, Böhringer T, Coray A, Goitein G, Grossmann M, Lomax A, Lin S and Jermann M 2001 A novel gantry for proton therapy at the paul scherrer institute *AIP Conference Procidings* **600** 13–17
[32] Zarifi S, Ahangari H T, Jia S B, Tajik-Mansoury M A, Najafzadeh M and Firouzjaei M P 2019 Bragg peak characteristics of proton beams within therapeutic energy range and the comparison of stopping power using the gate monte carlo simulation and the nist data *J. Radiother. Pract.* **19** 173–81
[33] Parodi K and Enghardt W 2000 Potential application of pet in quality assurance of proton therapy *Phys. Med. Biol* **45** 151–6
[34] Mashayekhi M, Mowlavi A A and Jia S B 2017 Simulation of positron emitters for monitoring of dose distribution in proton therapy *Reports of Practical Oncology and Radiotherapy* **22** 52–7